Investigation of path dependence in commercial lithium-ion cells for pure electric bus applications: Aging mechanism identification

Zeyu Ma [a, b], Jiuchun Jiang [a], Wei Shi [a], Weige Zhang [a, b], Chunting Chris Mi [b, *]

[a] National Active Distribution Network Technology Research Center, School of Electrical Engineering, Beijing Jiaotong University, No. 3 Shangyuancun Street, Haidian District, Beijing 100044, China
[b] DOE GATE Center for Electric Drive Transportation, Department of Electrical and Computer Engineering, University of Michigan, 4901 Evergreen Road, Dearborn, MI 48128, USA

HIGHLIGHTS

- Studied the path dependence of aging of lithium ion batteries.
- Considered the conditions of path dependence specific to Beijing pure electric bus.
- Demonstrated battery diagnostic approach for cell degradation using ICA and DVA.
- Cell degradation and its path dependence are illustrated in a quantitative manner.

ARTICLE INFO

ABSTRACT

There is a growing need to provide more realistic and accurate State of Health estimations for batteries in electric vehicles. Thus, it is necessary to research various lithium-ion cell aging processes, including cell degradation and related path dependence. This paper focuses on quantitative analyses of cell aging path dependence in a repeatable laboratory setting, considering the influence of duty cycles, depth of discharge (DOD), and the frequency and severity of the thermal cycle, as reflected in pure electric buses operated in Beijing. Incremental capacity analysis (ICA) and differential voltage analysis (DVA) are applied to infer cell degradation mechanisms and quantify the attributions to capacity fade. It was observed that the cells experienced a higher rate of aging at 80% DOD and an accelerated aging at 40 °C in the thermal cycling, as a result of possible loss of active material (LAM) in both electrodes, in addition to the loss of lithium inventory (LLI) and inhibited kinetics. The slight capacity fade from low-temperature extremes likely caused by LLI due to lithium plating, whereas the noticeable fade after the high-temperature excursion was likely caused by LAM and hindrance to kinetics. These results may lead to improved battery management in EV applications.

1. Introduction

Due to the energy crisis and the global commitment to reduce greenhouse gas emissions, advanced lithium-ion battery systems are currently being developed for electrical vehicles (EVs), hybrid electric vehicles (HEV), and smart grid applications. However, to satisfy the operation voltage and traction power needs, battery systems must now be designed for complex, larger-scale operations in multi-cell configurations. To avoid the adverse effect of cell inconsistency on battery pack performance, and to prolong the service life of both pack and cells, an advanced battery management system (BMS) plays a vital role in improving battery performance, safety, and reliability [1,2].

One of the most important key functions of a BMS is to achieve an accurate SOH estimation, which is beneficial not only for efficient energy management, but also for the diagnosis and prognosis of battery performance. In recent years, since SOH is often indicated by capacity fade and power fade, many approaches to estimating SOH are based on the estimation of battery parameters. Plett did extensive work to investigate the use of the extended Kalman filter (EKF) and sigma-point Kalman filter (SPKF) to estimate battery parameters and state, including resistance and capacity [3,4]. Xiong et al. [5] proposed a data-driven multi-scale EKF approach that is

* Corresponding author. Tel.: +1 313 583 6434; fax: +1 313 583 6336.
E-mail addresses: mazeyuhb@gmail.com (Z. Ma), chrismi@umich.edu, mi@ieee.org (C.C. Mi).

robust in estimating capacity and SOC of degrading battery. Kim et al. [6] combined dual extended Kalman filter (DEFK) and pattern recognition as an application of Hamming Neural Network to identify suitable battery model parameters for improved SOC/capacity estimation and SOH prediction. A support vector machine (SVM) algorithm is implemented and coupled with a dual filter consisting of an interaction of a standard Kalman filter and an Unscented Kalman filter by the authors in Ref. [7]. The authors in Ref. [8] presented an online battery SOH estimation method using the identified diffusion capacitance based on Genetic Algorithm. The "black box" based methods were also applied to estimate the battery capacity. The authors in Ref. [9] proposed an empirical capacity estimation model based on the Dempster–Shafer theory and the Bayesian Monte Carlo method for battery SOH estimation. Hu et al. [10] proposed an improved sample entropy based capacity estimator for prognostic and health management of Li-ion batteries. The aging datasets of eight cells under three different temperatures were used to establish and evaluate the estimator.

However, batteries' life and associated degradation mechanisms are strongly dependent on battery architecture, load profile, and control strategies [11]. Particularly, the influence of uncertainty in the load profile during the real-world battery operations have been ignored in most of these models, which may compromise effectiveness in real EV applications [11]. Thus, a greater understanding of aging processes including cell degradation and related path dependence in the conditions specific to EV or HEV applications is desired [12].

Unfortunately, the majority of cell tests are designed to evaluate cell behavior and degradation without the consideration of path dependence in the aging processes. Most of the analyses on cell degradation are ex suit and conducted by postmortem characterizations, which involves the destruction of cells [13]. The postmortem analysis may reveal the cause of degradation, but most of the analysis results do not provide temporal resolution and correlation with the underlying mechanism, which may lead to the extent of aging path-dependent [13]. Furthermore, they cannot be applied to the BMS for a better diagnosis of battery aging and SOH estimation.

To strive for more clarity on such issues, Dubarry et al. [12–15] recently used electrochemical characterization and analysis techniques, primarily analysis of incremental capacity (IC), i.e. $dQ/dV = f(V)$, to derive time-correlated degradation behavior under the cycle aging conditions to provide better understanding of the cell aging process. Honkura et al. [16] and Bloom et al. [17–19] preferred to use the analysis of differential voltage (DV), i.e. $dV/dQ = f(Q)$. Both these two in suit techniques can yield similar information for better understanding of the degree of cell degradation in a quantitative manner. Furthermore, since the IC curves and DV curves can be derived from the constant current charge curves, which can be easily obtained from the slow charge regime of EV, they have the potential to achieve better online diagnosis performance of battery aging.

The aging mechanisms of $Li_xMn_2O_4$ (LMO) based cells have been studied in the literature [20–27]. Most plausible aging mechanisms reported in the literature can be categorized into three types, including loss of active material (LAM), loss of lithium inventory (LLI) and degradation in kinetics (ohmic and faradic resistances) [14]. LAM can be induced by changes or even damage in the active material structure, or dissolution of transition metal Mn into the electrolyte [14,20–23]. The main origin of LLI could be due to the formation of solid-electrolyte interphase (SEI) layers or lithium plating [14,24–26]. The degradation in kinetics mainly arises from the slowing down of the charge transfer, or the reduction of electrode contact and electrolyte conductivity [14,27]. LLI commonly occurs when lithium-ions are partially consumed by parasitic reactions in the charge regime, resulting in the growth of the SEI layer on the negative electrode (NE) [14]. But LAM may occur in both charge and discharge regime that arises from the changes in both positive electrode (PE) and NE.

It should be noted that this study is carried out to quantify field-type aging path dependence in a repeatable laboratory setting while considering actual field conditions of pure electric bus applications in Beijing, but not to research the aging mechanisms of LMO-based cell. A set of aging path dependence studies have been initiated by Gering et al. [28] that focus on fundamental factors, including magnitude and randomness of power pulses, and magnitude and frequency of the thermal cycling. While those studies were based on a generalized consideration of the use of lithium-ion battery in PHEV-type applications, our work focuses on the quantitative analysis of aging path dependence associated with the conditions under which pure electric buses operate in Beijing. There will be more than 2000 electric buses operated in Beijing in the next few years. This study will be able to provide a more realistic and accurate SOH estimation and life prediction, as well as provide a basis for improving battery application and management in the Beijing pure electric bus. Due to the fixed operation route and mileage after each charge regime, the main aging factors in the Beijing pure electric bus involve the nature of duty cycles, DOD, and the frequency and severity of thermal cycles. Using the ICA and DVA techniques, these factors are studied in a controlled and repeatable laboratory setting to identify the path dependence of aging mechanisms by accounting for the influence of actual field conditions.

2. Experimental conditions

2.1. Aging path dependence

Aging path dependence is an important factor for EV or HEV applications in which batteries are used in dynamic, variable conditions. The sequence of aging conditions, as well as the nature of aging conditions, directly influences the rate of aging along the timeline [28]. Lithium-ion cells in a vehicle configuration will experience various combinations of usage and rest periods over a wide range of temperatures and SOC. The initial cell inconsistency, different series and parallel connections, and different locations in the vehicle can result in each cell in the battery pack working under different conditions, especially temperature. Therefore, each of the cells will experience a different aging path to a different final aging state.

A total of 100 $LiMn_2O_4$ battery modules (four 90 Ah cells are paralleled in one 360 Ah battery module) dissembled from a Beijing Olympic Games pure electric bus have been tested. It should be noted that electric buses from the Beijing Olympic Games have been operated for more than five years as Beijing Route No. 90 buses, and the battery packs used in these buses have been replaced once. A huge difference of capacity and ohmic resistance changes are presented in Fig. 1. The maximum difference of capacity and the ohmic resistance between the new battery modules are 10 Ah and 0.05 mΩ, respectively, but the maximum difference between the eliminated battery modules increased to 30 Ah and 0.216 mΩ, respectively. We also find that the rates of resistance increase and capacity fade are not related. There is high capacity fade in a battery module with a small increase in resistance, while a battery module with low capacity fade experiences a large increase in resistance. The cells are in different aging states throughout the different fade rates. Thus, it is inaccurate to estimate SOH based solely on capacity or resistance.

Two possible ways to regarding path dependence of cell aging are illustrated in Fig. 2, where the relative capacity loss is shown
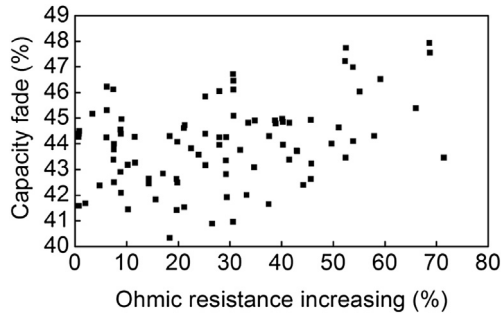
Fig. 1. Scatter plot of battery capacity fade with ohmic resistance increasing.

Fig. 3. The simplified testing profile of the No. 90 pure electric bus derived by principal component analysis.

against time, exhibiting four distinct aging regions under the different rearrangements of aging conditions. Path 1 is an idealized plot of the cell aging process. The reference extent of capacity loss is shown in the fourth region, in which the longest usage time is achieved. However, in a field-type application, a random rearrangement of aging stages is not guaranteed to result in an identical loss of capacity at the end of the fourth period. Similar to Path 2, the fourth period may arrive earlier, possibly due to the exposure of the cell to extremely high temperatures, which results in the realization of the reference extent of capacity loss in advance. Given such knowledge, through the control of working conditions such as temperature and SOC in a certain range, an optimal path would minimize cell degradation while meeting performance goals, thereby maximizing cell life [28]. In order to control the working conditions, a greater understanding of aging path dependence under the conditions specific to EV or HEV applications is desired. Due to the fixed operation route and mileage of the Beijing electric bus after each charge regime, the main aging factors considered for this study's experimental design include the influence of duty cycles, DOD, and the frequency and severity of thermal cycles in the Beijing pure electric bus service.

2.2. Duty cycle and DOD

In order to bridge the gap between laboratory test conditions and the actual operating conditions of pure electric buses in Beijing, we used the Beijing dynamic stress test (BJDST) schedule, which is derived from the operation data of the Beijing No. 90 electric bus, as the duty cycle in the thermal cycling. In our previous work, the one-year operation data of a Beijing No. 90 electric bus was analyzed using the principal components analysis while considering the power distribution of the electric bus during operation. Then, referring to the DST, the 900 s simplified BJDST was derived to reflect the operation characteristics of Beijing electric bus, as shown in Fig. 3 [29]. It is worth noting that the BJDST reveals a variety of information about the operation and utilization patterns of the electric bus, including the averag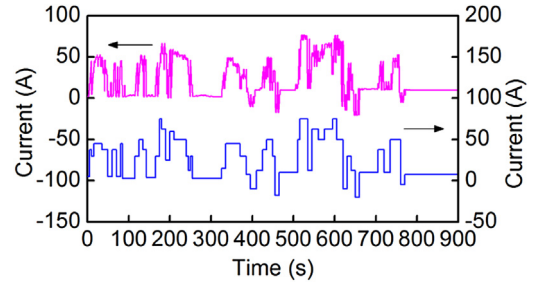e powers and their durations of idling, acceleration, constant speed and deceleration, the standard deviation of power distribution, and the minimum and maximum instantaneous powers. In Fig. 3, the upper curve, corresponding to the left Y-axis, shows the current profile of the BJDST derived by the principal components analysis; the lower curve, corresponding to the right Y-axis, shows the associated and simplified current profile of the BJDST for the battery test in the paper.

After a full charge regime and the completion of one cycle of the driving route, the SOC of the Beijing No. 90 electric bus's battery is between 60% and 70%. When the bus completes two cycles, the battery's SOC is between 30% and 40%. In order to simulate the characteristics of operation mileage and the number of operation cycles after each charge regime, we select two SOC ranges—50-100% and 20-100%—for the battery test in the discharge regime using the BJDST schedule.

2.3. Temperature

Cell performance in thermal excursions and thermal aging is an important subject that must be considered, because EVs are operated in a variety of extreme temperature conditions [30]. There are two aspects that affect the temperature conditions of the battery system in an EV: the weather condition of the city or region in which the EV operated, and the structural design and installation of the battery pack in the EV.

Fig. 4, which shows the temperature changes in Beijing from January 1, 2011 to June 30, 2012, provides the base temperature for the battery test. However, thermogenesis and thermolysis, which are two complex processes that occur in the cell during the charge and discharge regimes, result in different degrees of temperature increase when the cell is used at different rates and temperatures. Fig. 5(a) shows the changes in the cell's surface temperature during constant rate charge regimes at 25 °C and C/3, C/2 and 2C/3. The rise in the cell's surface temperature as a function of SOC at different charge rates follows the trend as expected: the higher the charge rate, the higher the increase in surface temperature. Fig. 5(b) shows
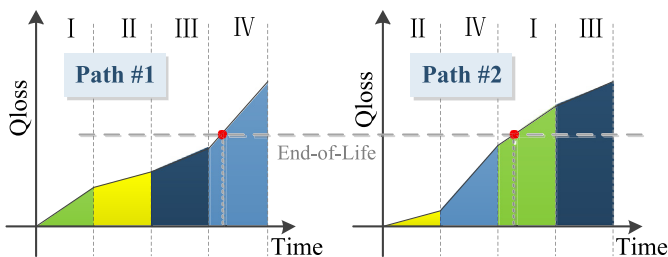

Fig. 2. Generalized diagram of two possible aging paths, illustrating four distinct periods of different aging conditions.
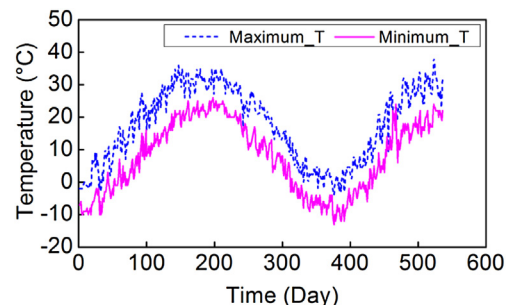

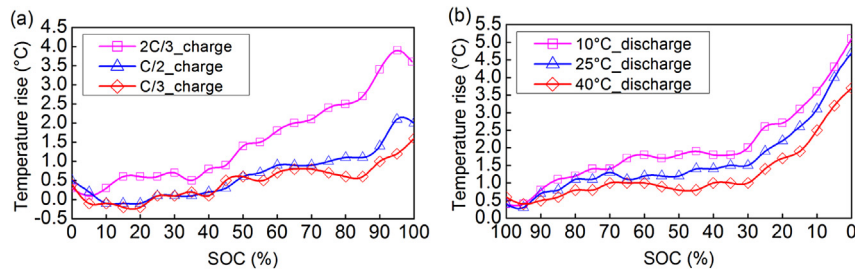Fig. 4. The daily temperature in Beijing from 1/1/2011 to 6/30/2012.

Fig. 5. The surface temperature rise of the cell (a) at 25 °C for the constant rate charge regimes at C/3, C/2 and 2C/3, (b) in the discharge regimes at 2C/3 at temperature of 10 °C, 25 °C and 40 °C.

the changes in the cell's surface temperature during the constant rate discharge regimes at 2C/3 and 10 °C, 25 °C and 40 °C. Since the ambient temperature increases, the polarization resistance — which includes both ohmic and faradaic resistance − decreases, leading to a decrease in heat generation, thereby resulting in a greater increase in the cell's surface temperature at 10 °C than at 40 °C.

Although the cell's surface temperature during the charge and discharge regimes at different rates and ambient temperatures does not rise substantially, partial cells in the battery pack may be exposed to extremely higher temperatures due to the battery's problematic structural design and ineffective cooling system. Thus, considering the weather conditions and the possibility of uneven thermal distribution in the battery pack, 10 °C, 25 °C and 40 °C are chosen as the temperature conditions in the isothermal thermal cycling. These temperatures, which are associated with the mean temperature of each month in Beijing, as shown in Table 1, aim to simulate the temperature conditions of the four seasons during which the electric bus is operated.

In accordance with the typical, real-world operation of the vehicle, the batteries will start out cool or cold, gradually warm up to normal temperatures at which they will operate for some time, and then cool down after the vehicle is turned off [28]. Therefore, we propose to quantify the effects of thermal excursions on lithium-ion batteries by accounting for extreme high and low temperatures (0 °C and 60 °C, respectively) in the field conditions.

3. Experimental

Eighteen 90 Ah commercial lithium-ion cells composed of a graphite negative electrode and an LMO positive electrode have been studied in this work. All of the $LiMn_2O_4$ cells were provided by the same manufacturer that supplied the cells chosen for the Beijing pure electric buses.

Using a series of charge and discharge regimes at C/3, the cells were all subjected to a conditioning process to determine the actual initial capacity. This process was not terminated until the capacity was stabilized within ±0.2% between two consecutive cycles. The cells can typically be conditioned within 3−6 cycles [12]. Subsequently, the cells were divided into nine groups and subjected to different types of thermal cycling and excursion at 50%, 80% and 100% DOD, respectively. Table 2 shows the matrix of test conditions, where temperature range refers to the ambient temperature surrounding the cells while in their environmental chambers.

Table 2
The matrix of cell tests for path dependence study.

Test condition	Test type	Number of cells	Temperature range	DOD	Duty cycle
1	Isothermal thermal cycling	2/2	10 °C	50%/80%	BJDST
2	Isothermal thermal cycling	2/2	25 °C	50%/80%	BJDST
3	Isothermal thermal cycling	2/2	40 °C	50%/80%	BJDST
4	Mild thermal cycling	2/2	10−40 °C	50%/80%	BJDST
5	Sever thermal excursion	2	0−60 °C	100%	Constant current

From the first to the fourth test condition, a total of 16 cells in eight groups were selected from the same batch and employed in the path dependence study. All cells in these tests were recharged using a constant current (CC) at C/3 step to 4.2 V, followed by a constant voltage (CV) step at 4.2 V until the termination current of C/20 was reached [12], and then discharged using the BJDST schedule. There were two groups in each test condition in which the cells were discharged until the 50% and 80% DOD were reached, respectively. The cells were subjected to isothermal thermal cycling at three selected temperatures (10 °C, 25 °C and 40 °C) in the first three test conditions. In the fourth test condition, the cells were subjected to mild thermal cycling at a dynamic temperature (DT), where the temperature was changed repeatedly in a certain frequency to simulate a season change in which 10 °C was maintained for two days, then changed to 25 °C for one and a half days, and then 40 °C for two days. For every 50 cycles at 50% DOD and for every 42 cycles at 80% DOD, capacity characterization was performed at 25 °C to investigate the capacity fade in the first four test conditions. The capacity at a rate of C/3 was measured using 5 cycles. In order to reach a thermal equilibrium for the cell before and after capacity testing, the cell was allowed to rest for 4 h when the temperature was changed. Rest time between the charge and discharge regime was 2 h in the capacity test.

In terms of the fifth test condition, two cells were selected from another batch and subjected to additional reference performance tests (RPTs) at C/20, C/3, C/2, 2C/3 and 1C cycle regimes at different temperatures in the following excursion: 25 °C, 0 °C, 25 °C, 40 °C, 60 °C, and 25 °C. Whenever the temperature changed, the cell was allowed to rest for 4 h in order to reach a thermal equilibrium. In

Table 1
Selected temperatures for the battery test associated with the mean temperature of each month in Beijing.

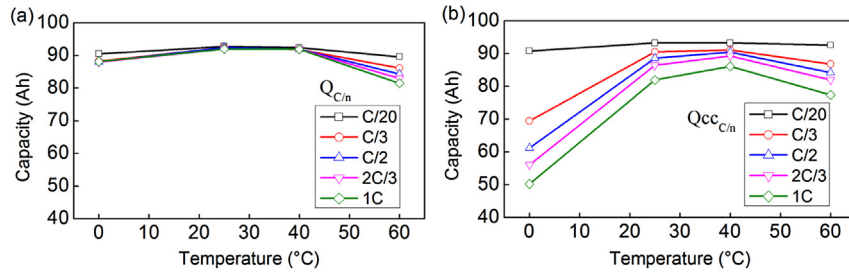| Month	1	2	3	4	5	6	7	8	9	10	11	12
Mean temperature/°C	−4.6	−2.2	4.5	13.1	19.8	24	25.8	24.4	19.4	12.4	4.1	−2.7
Selected test temperature/°C	10	10	10	25	25	40	40	40	25	25	10	10

Fig. 6. (a) Capacity retention $Q_{C/n}$ and (b) retention of charge return $Qcc_{C/n}$ in constant current charge regime as a function of rate in the thermal excursion from 0 °C to 60 °C.

each isothermal regime, an RPT with charge and discharge cycles at five different rates and 100% DOD was conducted. With the exception of the cell cycled at C/20, which was charged using a CC step to 4.2 V, the cell cycled at other rates was charged using the CC–CV regime at different rates. A 2-h rest period was imposed between any charge or discharge regime to determine the rest cell voltage (RCV) at the end-of-charge (EOC) or the end-of-discharge (EOD). After the rest, the residual capacity in the cell at the EOD was measured subsequently by a CC step at C/20 until 3 V (the cutoff voltage) was reached again. Then, the cell was allowed another 2-h rest to determine the RCV, which corresponded to the start point of the next regime and denoted as the beginning-of-charge (BOC). There were three reference points (the initial, midpoint and final RPTs) at 25 °C to analyze and quantify the effects of the low- and high-temperature branch excursions (LTBE and HTBE) [30].

4. Results

4.1. Cell performance at different isothermal regimes in the thermal excursion

Fig. 6(a) shows the capacity retention $Q_{C/n}$ as a function of temperature and rate in the thermal excursion. This follows the trend from 0 °C to 40 °C as expected: the higher the temperature, the better the kinetics, and the larger the capacity. However, the difference in capacity between C/20 and 1C decreases as the temperature rises from 0 °C to 40 °C, but increases as the temperature rises from 40 °C to 60 °C. Capacity fade occurred slightly at 40 °C, but more significantly at 60 °C. Fig. 6(b) presents the retention of charge return $Qcc_{C/n}$ in the CC charge regime as a function of temperature and rate in the thermal excursion. Below 25 °C, due to the limited voltage range imposed by the test, which ensures that the cell stays within the electrolyte stability range [30], the cell could only be charged partially at rates higher than C/20. Overall, the $Qcc_{C/n}$ follows the same trend as $Q_{C/n}$ up to 60 °C.

Fig. 7 displays the evolution of RCVs in the discharge regimes in the thermal excursion. There are three sets of curves displayed in

the plot: the first set is the RCV_{BOD}, the second is the RCV_{EOD} at the cutoff voltage, and the third is the RCV_{BOC} after residual capacity measurements. The RCV_{BOD} is similar at all rates, indicating that the CC–CV charge protocol ensures that the cell could be recharged at nearly the same capacity. The evolution of the RCV_{EOD} follows the same trend as that of $Q_{C/n}$. After the residual capacity measurements, the RCV_{BOC} returns to similar value for at all rates. Thus, the protocol in the test regimes warrants the comparison of capacity variations among various test regimes valid and free from bias from prior regimes [30].

4.2. Cell performance at 25 °C through the thermal excursion

The evolutions of the three RPTs at 25 °C are useful indicators for identifying the extent of cell degradation. The cell capacity is 92.75 Ah at C/20 and 92 Ah at 1C in the initial RPT at 25 °C. Fig. 8 shows the evolution of cell capacity as a function of rate for the three RPTs at 25 °C. The LTBE leads to 0.4% capacity fade, which means the cell capacity fades to 92.4 Ah. The HTBE results in 6.3% capacity fade; in the other words, the cell capacity fades to 86.6 Ah. The Peukert curves of the three RPTs are almost parallel. Thus, the capacity fade is unlikely a result of kinetic degradation.

4.3. Cell capacity fade in different thermal cycling

Fig. 9 exhibits the capacity fades of the cells cycled at different temperature conditions in different thermal cycling, which are measured from the capacity test using the C/3 rate at 25 °C as a function of the cycle number. The charge capacity fade of the cell (#13) cycled at 50% DOD and 40 °C is denoted as Z13-C(DOD50_T40) in the figure, for example. Fig. 9(c) shows that the cells cycled at 40 °C experience three stages in the cycle aging, while the other cells are still in the second stage. In the first stage, the cell undergoes the activation process for up to 100 cycles. The capacity remains intact and even increases slightly in the beginning, before decreasing to the initial value in other thermal cycling. In the second stage, the capacity decreases steadily for up to 350
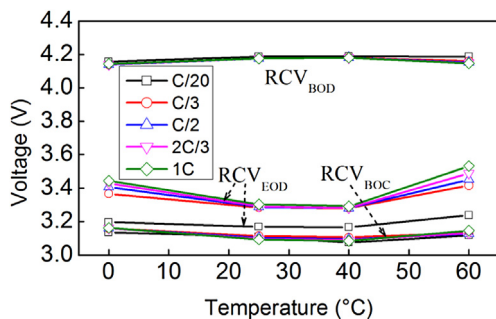

Fig. 7. Rest cell voltages in the discharge regimes as a function of rate in the thermal excursion from 0 °C to 60 °C.
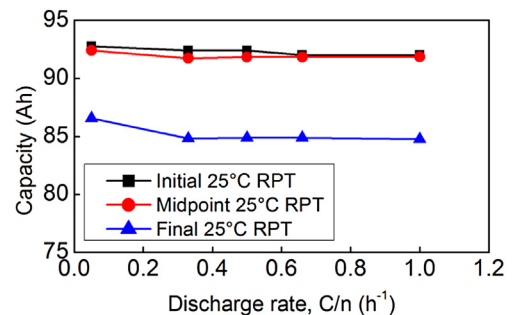

Fig. 8. Peukert behavior of the cell determined from the initial, midpoint and final RPTs at 25 °C.
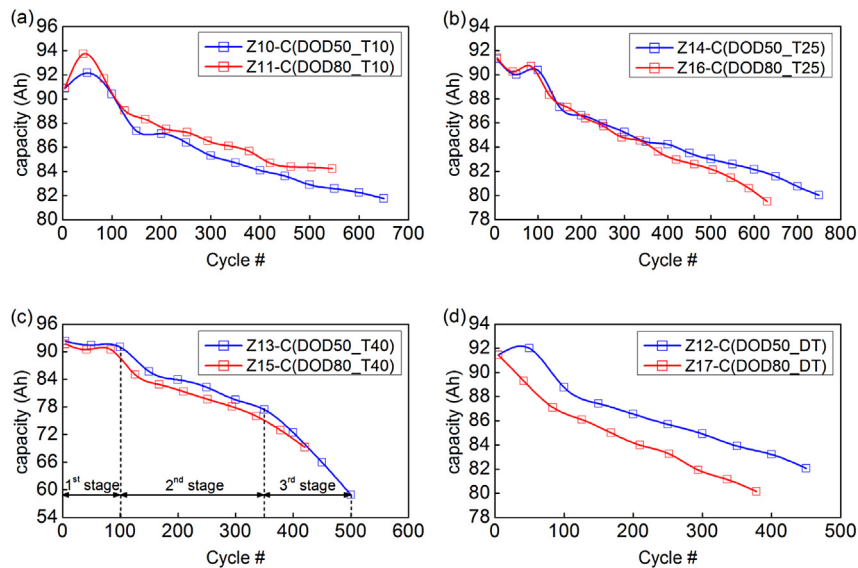
Fig. 9. Capacity fade of the cells (a) cycled at 10 °C, (b) cycled at 25 °C, (c) cycled at 40 °C, (d) cycled at dynamic temperature in different thermal cycling, measured from capacity testing using C/3 rate at 25 °C, as a function of the cycle number.
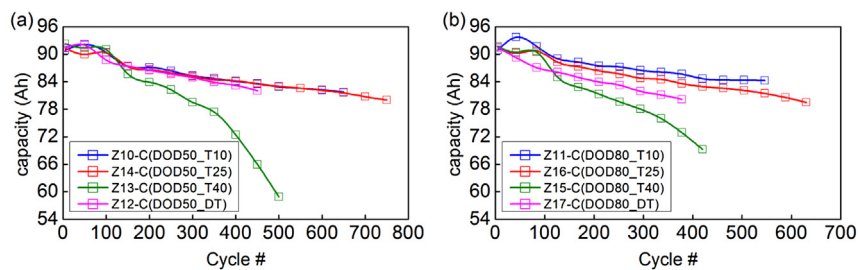

Fig. 10. Capacity fade of the cells (a) cycled at 50% DOD, (b) cycled at 80% DOD in different thermal cycling, measured from capacity testing using C/3 rate at 25 °C, as a function of the cycle number.

cycles. Beyond 350 cycles, the capacity loss accelerates in the third stage. Fig. 9(b) shows that the cells cycled at 25 °C at different DOD fade at almost the same rate for up to 350 cycles. The cell cycled at 80% DOD shows slightly more capacity fade than the cell cycled at 50% DOD. This phenomenon is also found in the cells cycled at other temperature conditions, excluding the cells cycled at 10 °C. This is likely because the actual capacity of the cell cycled at 10 °C and 80% DOD is slightly more than the cell cycled at 10 °C and 50% DOD after the activation stage.

Fig. 10 exhibits the capacity fades of the cells cycled at different DOD in different thermal cycling. As expected, the cells cycled at 40 °C show the fastest rate of capacity fade. The cells cycled at 50% DOD and the other three temperature conditions fade at nearly the

same rate, as exhibited in Fig. 10(a). The fade rate of the cells cycled at 80% DOD increase with the rise of temperature, as shown in Fig. 10(b).

5. Discussion

5.1. IC and DV analysis

The IC curve is derived from a capacity change associated with a successive voltage step (dQ/dV) in the charge or discharge voltage–capacity curve. Each IC peak in the IC curve, representing an electrochemical process that takes place in the cell, has a unique shape, intensity and position [15]. Any change in position and shape
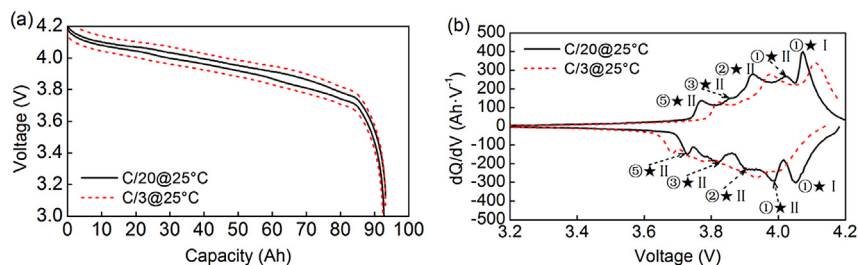

Fig. 11. (a) Voltage–capacity curves and (b) IC signatures of the charge and discharge regimes at C/20, C/3 and 25 °C.
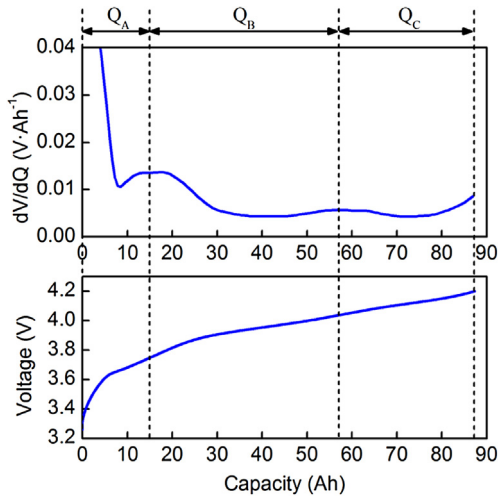
Fig. 12. Voltage–capacity curve and related differential voltage signature of the constant current charge regime at C/3 and 25 °C.

of an IC peak is a symptom of cell aging. Fig. 11 presents the voltage–capacity curves and related incremental capacity signatures of charge and discharge regimes at C/20, C/3 and 25 °C. The IC peaks observed in the IC curves correspond to the staging in the graphite negative electrode, convoluted with phase transformation on the positive electrode [12–15]. In the NE, the lithium intercalation transforms C to LiC_6 in at least five distinct staging processes [12,13,15], noted as ⑤-①. In the PE, two phase transformations take place in $LiMn_2O_4$ at 4.1 V and 4.0 V, respectively [12,13], noted as I and II. Due to the distinct staging processes in the NE, the IC peak corresponding with reaction II in the PE is split into three peaks, as shown in the IC curve (black and solid line) in Fig. 11(b). The same phenomenon happens in the NE. Thus, the peak indexed as ①★I represents reaction ① in the NE convoluting with reaction I in the PE. The IC curves show greater sensitivity than the conventional charge and discharge curves that allow us to probe any gradual changes of cell behavior during the thermal aging.

In order to track the SOH and cell fade, the IC curves are achieved by charging or discharging the cell at a very low rate such as C/25, which ensures a more accurate understanding of aging mechanisms [14]. However, the charging current of the cell is generally larger than C/25 in field-type applications. It should also be noted that it is difficult to obtain accurate IC curves from the dynamic and complex discharging process that depend on the driving cycles. The electric bus is generally recharged in a charging station using the traditional CC–CV regime. In this study, the aging mechanisms were mainly identified using the IC curves derived from C/3 charge curves, which aimed to make it easier to be applied to the BMS for the EV applications.

We found that there are only three obvious IC peaks in the IC curve of charge regime at C/3 (red and dashed line in the web version) shown in Fig. 11(b), noted as ①★I, ②★II, ⑤★II, respectively. The area under each peak represents the whole incremental capacity involved in the associated reaction. Although IC curves may help to better understand cell degradation, contribution quantification of capacity fade might be easier to accomplish using the DV curves. Fig. 12 shows the voltage–capacity curve and related differential voltage signature of the CC charge regime at C/3 and 25 °C. In the DV curve, those staging phenomena become valleys while the DV peaks represent non-stoichiometry in the single-phase regions (solid solution) [14]. The DV curve is naturally divided into three regions by the DV peaks, where each region corresponds to the capacity of a phase transformation involved in the reaction. The charging capacity corresponding to each region, noted as Q_A, Q_B and Q_C, are associated with the areas under the peaks ⑤★II, ②★II and ①★I, respectively, in the IC curve. Next, the aging mechanism of the cell can be similarly analyzed by investigating the changes in Q_A, Q_B and Q_C [31]. It should be noted that the fidelity of the IC and DV curves are sensitive to the resolution of the data acquisition system [12]. Thus, in this study, the IC and DV curves are smoothed out to remove noise using the Savitzky–Golay filter with a third-order polynomial curve piecewise with a moving window.

5.2. Effect of temperature on the cell capacity fade in different thermal cycling

Fig. 13 shows the comparison of IC curves for the cells cycled at 40 °C, 10 °C and 50% DOD in different thermal cycling, which are derived from the charge regimes in the capacity test using C/3 rate at 25 °C, as a function of the cycle number. It is important to realize that the IC peak ①★I is a useful status indicator for lithium content and intercalation kinetics in the graphite NE during charging, and the peak's changes are mainly due to the LLI process [12–15]. The degradation of the IC peak ⑤★II is likely a result of the LAM process [12–15]. In the case of the cell cycled at 40 °C and 50% DOD, the peak positions increase significantly in the IC curves, indicating a significant increase in polarization in the cell, as shown in Fig. 13(a). After 450 cycles, the polarization increases to such an extent that the reaction corresponding to peak ①★I is not completed or does not even occur at the charging cut-off voltage of 4.2 V. The related phase transformation process is performed in the CV charge step, thus the peak ①★I disappears from the IC curve, as indicated by * in Fig. 13(a). Finally, the process results in LLI in the CC charge step. It should be noted, however, that the capacity loss in the CC charge step is more than the total capacity loss, because the charge capacity in the CV charge step increases with the expanded period in the CV charge step. Thus, partial capacity loss due to LLI in the CC charging can be recovered in the CV charging. It can be seen clearly that not only the intensities of the three peaks decrease, but the
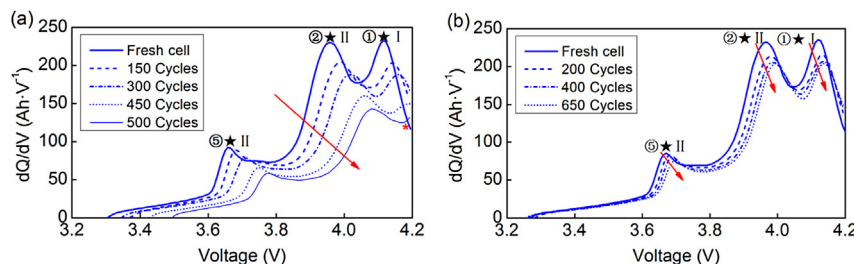

Fig. 13. Evolution of the IC curves for the cells cycled at (a) 40 °C and 50% DOD, (b) 10 °C and 50% DOD in different thermal cycling, derived from the charge regimes in capacity testing using C/3 rate at 25 °C, as a function of the cycle number.
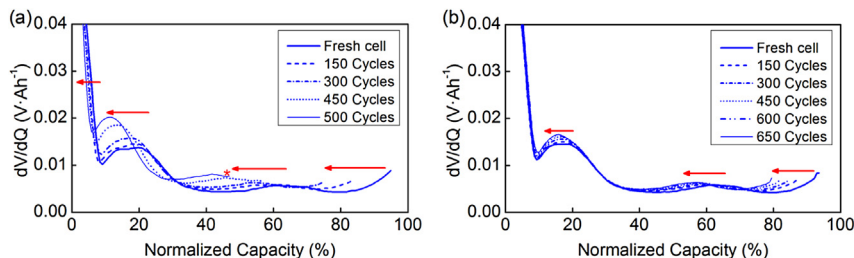
Fig. 14. Evolution of the DV curves for the cells cycled at (a) 40 °C and 50% DOD, (b) 10 °C and 50% DOD in different thermal cycling, derived from the charge regimes in capacity testing using C/3 rate at 25 °C, as a function of the cycle number.
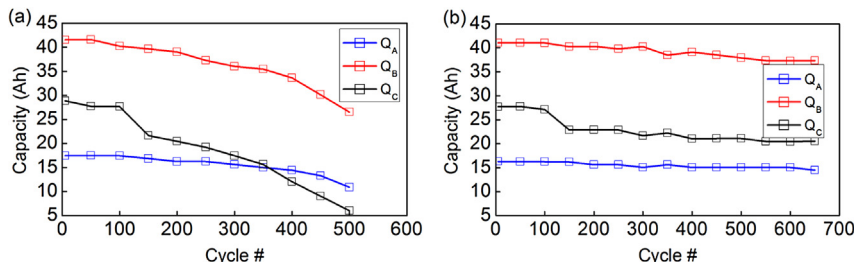

Fig. 15. Evolution of Q_A, Q_B and Q_C for the cells cycled at (a) 40 °C and 50% DOD, (b) 10 °C and 50% DOD in different thermal cycling, derived from the DV curves, as a function of the cycle number.

intensity of peak ①★I decreases more than the others, implying that the capacity fading also comes from an LLI in addition to a possible LAM. In the case of the cell cycled at 10 °C and 50% DOD, the peak positions were gradually shifted as a result of increasing polarization, but not to the same degree as the cell cycled at 40 °C. The interfacial kinetics are slowed, as indicated by the broadening of peak ⑤★II, which may be related to the SEI destabilization and the disorder of the graphite surface over aging [15]. The intensity of the three peaks has been diminishing obviously as well, suggesting

that the capacity fading mainly comes from LLI besides a possible LAM.

We can obtain the same conclusion from the DV curves [16–19], as shown in Fig. 14. The evolution of the DV curves also indicates that an LAM has occurred [14]. Furthermore, it is easier to quantify the respective losses in capacity corresponding to the three peaks in the IC curves using the DV analysis. Fig. 15 presents the evolution of Q_A, Q_B and Q_C for the cells cycled at 40 °C, 10 °C and 50% DOD in different thermal cycling, which are derived from the DV curves as a
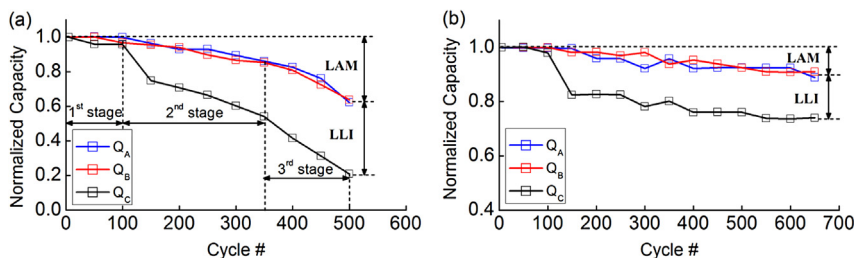

Fig. 16. Evolution of normalized Q_A, Q_B and Q_C for the cells cycled at (a) 40 °C and 50% DOD, (b) 10 °C and 50% DOD in different thermal cycling.
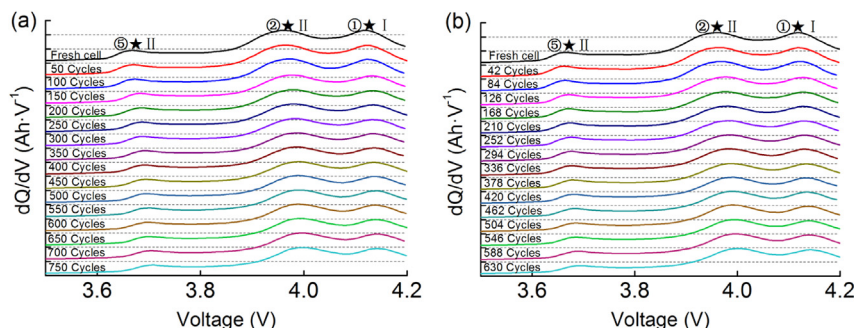

Fig. 17. Evolution of the IC curves for the cells cycled at (a) 50% DOD and 25 °C, (b) 80% DOD and 25 °C in the thermal cycling, derived from the charge regimes in capacity testing using C/3 rate at 25 °C, as a function of the cycle number.

Fig. 18. Evolution of the DV curves for the cells cycled at (a) 50% DOD and 25 °C, (b) 80% DOD and 25 °C in the thermal cycling, derived from the charge regimes in capacity testing using C/3 rate at 25 °C, as a function of the cycle number.
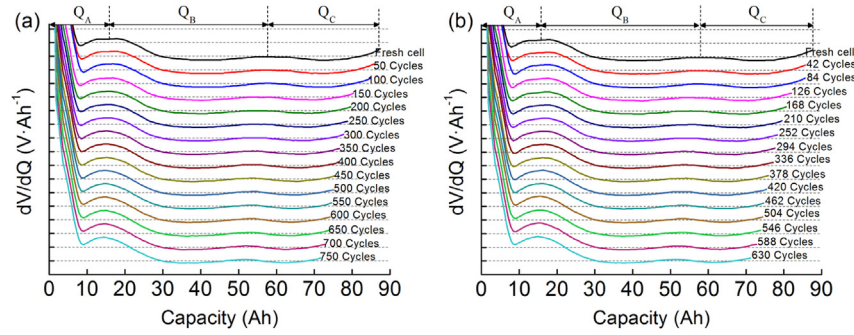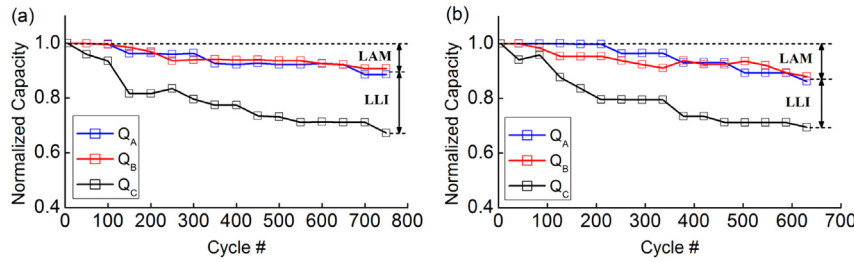

Fig. 19. Evolution of normalized Q_A, Q_B and Q_C for the cells cycled at (a) 50% DOD and 25 °C, (b) 80% DOD and 25 °C in the thermal cycling.

function of the cycle number. Q_A, Q_B, and Q_C decrease significantly. Q_A and Q_B decrease at nearly the same rate, indicating that the capacity loss arises from the LAM in the NE. Q_C decreases at an even higher rate, indicating that an LLI exists in addition to the LAM. Fig. 16 exhibits the evolution of normalized Q_A, Q_B and Q_C. In the case of the cell cycled at 40 °C and 50% DOD, there are three stages of LAM through about 500 cycles, as shown in Fig. 16(a). This corresponds exactly to the three stages of cycle aging. The capacity fade due to LLI follows a linear relationship throughout nearly all the stages of cycle aging, as derived from the test data. We can see that the fade curve of normalized Q_C is almost parallel to the curves of normalized Q_A and Q_B. Thus, the increasing rate of LAM in the

third stage accelerates the capacity fade. In high temperatures, Mn^{2+} can be easily dissolved into electrolytes, resulting in the loss of electrolytes and LAM, as well as structural damage to the cathode [25–27]. For the graphite-NE based cell, Mn^{2+} may be conducted to the NE and reduced on the surface due to the lower potential of NE, consequently thickening the SEI layer and resulting in a continuous capacity loss and polarization increase [25–27]. Thus, we have reason to believe that an LAM occurs in both electrodes in the third stage of cycle aging at 40 °C.

In the case of the cell cycled at 40 °C and 50% DOD, where 50.6% of the capacity loss in the CC charge step was measured after 500 cycles, the capacity fade from LLI contributes 18.5% of the capacity
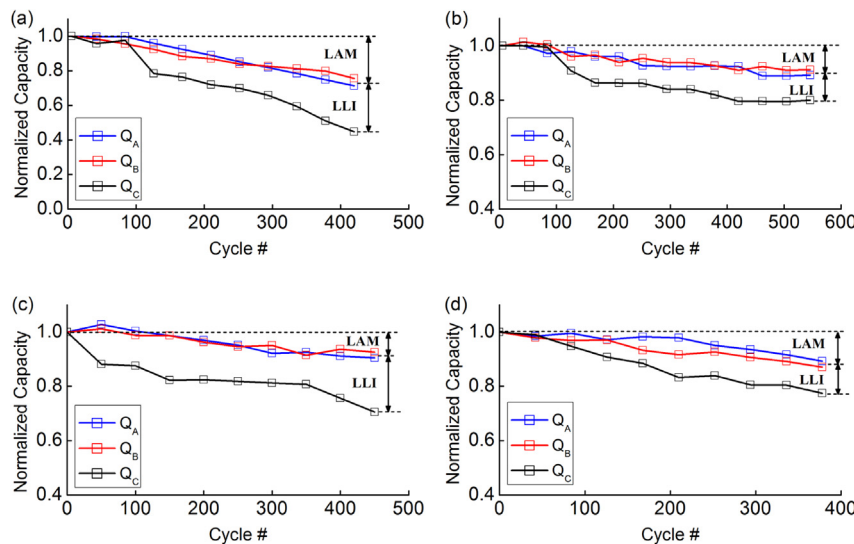

Fig. 20. Evolution of normalized Q_A, Q_B and Q_C for the cells cycled at (a) 40 °C and 80% DOD, (b) 10 °C and 80% DOD, (c) dynamic temperature and 50% DOD, (d) dynamic temperature and 80% DOD in the thermal cycling.

Table 3
Statistical integrated values of capacity loss and related contributions of the cells cycled at different thermal conditions.

Temperature/°C	10	25	40	Dynamic (10–40)
DOD/%	50/80	50/80	50/80	50/80
Capacity fade in CC charging/%	15/12.8	17.6/18.7	50.6/35.3	15.2/15.4
LAM contribution/%	8.6/6.4	8.6/11.1	32.1/22.9	7.2/10.8
LLI contribution/%	6.4/6.4	9/7.6	18.5/12.4	8/4.6

loss. The remaining 32.1% is a result of LAM. In other words, the capacity loss from LAM contribution accounts for 63.4% of the total capacity loss (32.1%/50.6% = 63.4%). For the cell cycled at 10 °C and 50% DOD, 15% of the capacity loss in the CC charge step after 650 cycles comprises about 6.4% of the LLI contribution, while the remaining 8.6% is a result of LAM. This means that the capacity fade from LAM accounts for 57.3% of the whole fade. It should be noted that the larger capacity loss is a result of the LAM in the cell cycled at 40 °C. This may provide a stronger support for the hypothesis that LAM occurs in both PE and NE of the cell cycled at 40 °C. Thus, in terms of the LMO-based cell chosen for the Beijing pure electric bus application, the thermal management should be designed carefully to prevent part of the cells in the battery system from experiencing accelerated aging at high temperatures.

5.3. DOD effect on the cell capacity fade in different thermal cycling

Fig. 17 shows the comparison of IC curves for the cells cycled at 50% DOD, 80% DOD and 25 °C in different thermal cycling. The peak positions of all cells cycled at 50% DOD and 80% DOD were shifted slightly, indicating that there is no obvious increase of polarization in the cell. In these two cases, the intensities of the three peaks have been diminishing, suggesting that the fade is a result of the LLI and LAM. Fig. 18 shows the evolution of DV curves for the cells cycled at 50% DOD, 80% DOD and 25 °C in the thermal cycling. We can then quantify the respective capacity losses of the three peaks by investigating the changes in Q_A, Q_B and Q_C, which are derived from the DV curves, as shown in Fig. 19. In both cases, Q_C decreases at a rate higher than Q_A and Q_B, indicating that an LLI exists in addition to the LAM.

In the case of the cell cycled at 50% DOD, where 17.6% of the capacity loss in CC charging was measured after 750 cycles, the capacity fade from LLI makes up 9% of the capacity loss. The remaining 8.6% is a result of the LAM. In other words, the capacity loss from the LAM contribution accounts for 48.9% of the total capacity loss. For the cell cycled at 80% DOD, where 18.7% of the capacity loss in CC charging was measured after 630 cycles, the capacity fade from LLI comprises about 7.6% of the capacity loss, while the remaining 11.1% is a result of LAM. This means that the capacity fade from LAM accounts for 59.4% of the total capacity

fade. Greater capacity loss results from the LAM in the cell cycled at 80% DOD. This may account for the phenomenon in which the cell cycled at 80% DOD shows a slightly higher rate of capacity fade than the cell cycled at 50% DOD after 350 cycles.

Fig. 20 presents the evolution of normalized Q_A, Q_B and Q_C for the cells cycled under the other four conditions. The capacity loss and related contributions of the cells cycled under eight different test conditions are integrated in Table 3. It can be observed that greater capacity loss comes from the LAM in the cell cycled at 80% DOD than the cell cycled at 50% DOD at different temperatures, which explains the slightly higher rate of capacity fade for the cell cycled at 80% DOD, with the exception of the cell cycled at 10 °C. This may be due to the greater actual capacity of the cell cycled at 80% DOD and 10 °C, as shown in Fig. 9(a), where we can see a greater increase in capacity in the first stage. When the cell is discharged to a lower potential—in other words, a higher DOD—lithium-ions accumulate on the surface of the PE due to the much faster diffusion rate of Li$^+$ in electrolytes than in positive material. Then, Mn^{4+} is reduced to Mn^{3+}, and Jahn–Teller distortion is induced, which leads to the volume change of positive material and, finally, capacity fade [23,24]. Furthermore, the disproportionate dissolution of Mn^{2+} may be induced by Mn^{3+}, also resulting in capacity loss [26]. It is possible that LAM also occurs in the PE, in addition to in the NE, which results in higher capacity fade in the cell cycled at 80% DOD. Thus, due to the fixed operation route and mileage of the Beijing electric bus after each charge regime, it is easy to control the DOD of the battery to meet the mileage goals of the electric bus and to extend the cycle life of the battery through the reasonable arrangement of charging and departure regimes in the charging station.

5.4. Cell capacity fade in the thermal excursion

The cell was in the same state at BOD at different temperature in the thermal excursion, which is indicated by the consistency of RCV$_{BOD}$, as shown in Fig. 7. The subsequent drop in initial voltage due to IR, which is proportional to the ohmic resistance in the polarization, should be used to trace ohmic resistance variations in the thermal excursion. Fig. 21(a) shows the cell voltage after the initial IR drop in the discharge regime as a function of rate at different temperatures. The voltage follows the linear relationship with rate, as expected from Ohm's Law. The ohmic resistance for the cell exposed to each temperature is derived from the slope of the curve. Fig. 21(b) presents the logarithmic ohmic resistance as a function of reciprocal temperature in the Arrhenius plot. If the thermal activation process of the cell at different temperatures were in the same way, lnR should follow the linear relationship with $1/T$, as expected from the Arrhenius equation [30]. Thus, the non-linear correspondence suggests that the ohmic resistance change, which depends on temperature, is more complicated than expected, and not simply based on electrolyte conductance.
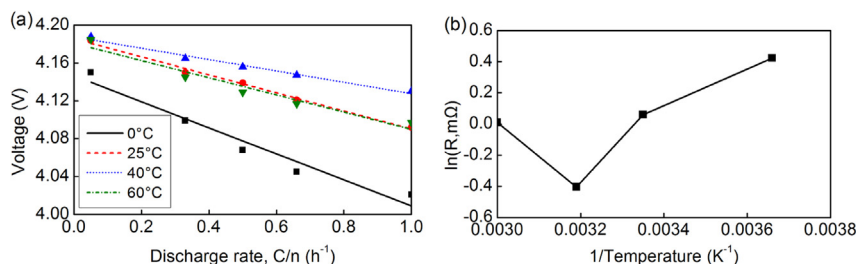

Fig. 21. (a) Cell voltage after the initial IR drop as a function of rate at different temperatures. (b) The derived logarithmic ohmic resistance as a function of reciprocal temperature is shown in the Arrhenius plot.
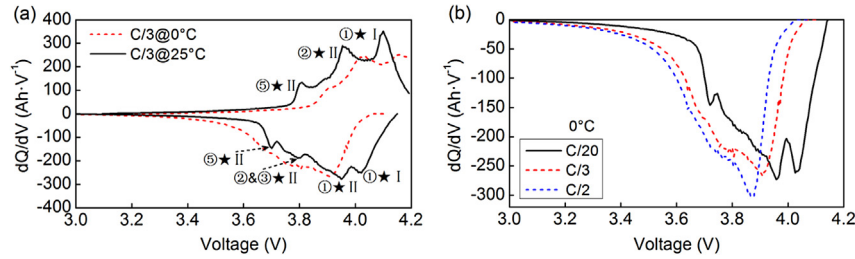
Fig. 22. (a) IC curves of the charge and discharge regimes at 0 °C, 25 °C and C/3. (b) IC curves at 0 °C for the discharge regimes at C/20, C/3 and C/2.
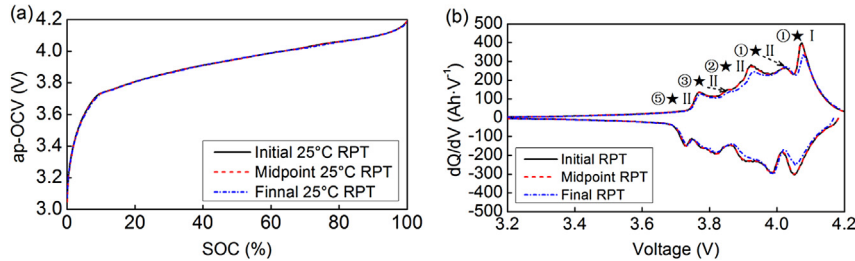

Fig. 23. (a) ap-OCV = f(SOC) curves for the initial, midpoint and final RPTs at 25 °C and (b) the corresponding IC curves at C/20.

Fig. 22(a) shows the IC curves of charge and discharge regimes at 0 °C, 25 °C and C/3. Due to the effects of polarization, the IC curve was shifted to a higher voltage at a lower temperature, where the peak ①★I was incomplete, and the shape, width and intensity of all the peaks changed. In the charge regime, the peak ⑤★II can be used to reflect the Li intercalation kinetics in the graphite NE. At the lower temperature, the peak ⑤★II becomes broader and lower, indicating that the Li intercalation kinetics in the graphite NE have been impeded, which leads to a longer time-resolved extent of reaction [12]. However, the related capacity does not change, indicating that the capacity accessibility of the NE is not retarded. Fig. 22(b) presents the IC curves at 0 °C for the discharge regimes at C/20, C/3 and C/2. The kinetics are impeded more severely due to the increase of rate at low temperatures. Since we can only measure the cell voltage on the surface of active material, the voltage suggests that reaction ①★II has already occurred, whereas the material composition in the core remains at reaction ①★I and needs to catch up with the surface reaction. Thus, peak ①★II becomes broader and starts to overlap with peak ①★I. Since a similar "Domino effect" is induced by the large potential difference between the surface and the core of active material, the following reaction needs to catch up with the surface reaction, which leads to all following peaks overlap with peak ①★I. However, the intensities of IC curves for all rates near the cutoff voltage are close to 0 Ah V^{-1}, indicating that the reaction is almost completed. Thus, the polarization change should not significantly impact the capacity retention.

The cell presented an obvious 6.7% capacity fade from the initial to the final RPT at C/20 through the thermal excursion, including 0.4% fade from the LTBE and 6.3% fade from the HTBE, as shown in Fig. 8. To track the SOH in the thermal excursion, the approximate OCV−SOC curves and corresponding IC curves related to the three RPTs at 25 °C are compared in Fig. 23. There is no noticeable difference in the approximate OCV−SOC curves, as seen in Fig. 23(a), but an obvious change is observed in the corresponding IC curves, as seen in Fig. 23(b), indicating that the capacity fade may have occurred after the thermal excursion. There is almost no difference between the IC curves at the initial and the midpoint, indicating that a slight fade does not result from the LAM after the LTBE. The capacity fade is likely due to the LLI, which is induced by metallic Li plating on the NE [32]. The Li plating could become passivated or consumed by the SEI formation, subsequently leading to capacity loss related to LLI [30]. In the discharge regime, if Li plating already occurred in the charge regime, a sharp peak at the beginning of the discharge is expected because metallic Li, which is highly activated, can easily become involved in the reaction. A sharp peak cannot clearly be observed in the IC curve at C/20, but a sharp peak is observed at higher rates (as noted by *), especially at 1C, as shown in Fig. 24(a). This may explain the capacity fade observed after the LTBE. There is a noticeable difference between the IC curves at the midpoint and the final. The shape of peak ⑤★II remains the same, indicating that LAM does not occur in the NE. However, the other peaks involved in reactions I and II have decreased, suggesting that a possible LAM has occurred in the PE due to the dissolution of Mn
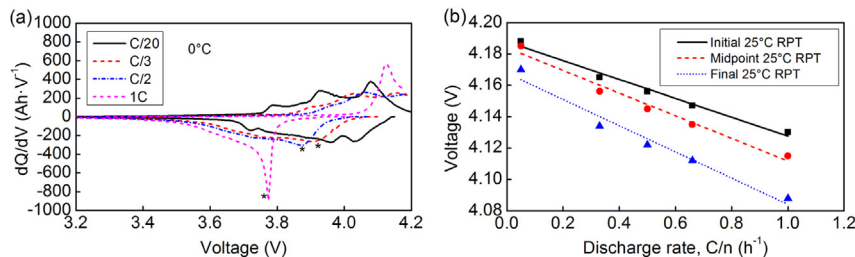

Fig. 24. (a) IC curves of the 1/20C, 1/3C, 1/2C and 1C cycles at 0 °C. (b) Cell voltage after the initial IR drop as a function of rate for the initial, midpoint and final RPTs.

at the high temperature. The ohmic resistances for the three 25 °C RPTs can be derived from the slopes of the curves, as shown in Fig. 24(b). The ohmic resistance for the final RPT is slightly higher than those of the other two, suggesting that the fade after the HTBE also could be a kinetic issue due to the increase of ohmic resistance.

6. Conclusion

This paper quantitatively illustrates a detailed analysis of cell degradation and its related path dependence in the conditions specific to the Beijing pure electric bus, focusing on the influence of duty cycles, DOD, and the frequency and severity of thermal cycles. A referred battery diagnostic approach using ICA and DVA to investigate cell fade and related path dependence is demonstrated. Although the aging mechanisms of LMO-based cells have been studied in the literature, our work provides additional detailed analyses to quantify the attributes to the capacity fade.

Our results show that the cells experience a higher rate of aging at 80% DOD and an accelerated aging at 40 °C in the thermal cycling. It is possible that LAM occurs in both the PE and the NE as a result of the Jahn–Teller distortion when the cell is discharged to a lower voltage, in addition to the LLI. The high temperature could induce LAM in both electrodes, in addition to LLI and inhibited kinetics from SEI growth, due to the dissolution of Mn via a disproportionation reaction. Capacity fade is observed in the thermal excursion that includes extreme temperatures. The slight capacity fade from low-temperature extremes seems related to Li plating. The noticeable fade after the high-temperature excursion seems to result from the loss of active materials, SEI formation on the positive electrode, and the hindrance to kinetics. The results of this study can be directly employed to design and optimize lithium-ion battery management technologies for future electric vehicle applications.

Acknowledgments

References

[1] R. Xiong, F. Sun, X. Gong, H. He, J. Power Sources 242 (2013) 699–713.
[2] R. Xiong, F. Sun, X. Gong, C. Gao, Appl. Energy 113 (2014) 1421–1433.
[3] G.L. Plett, J. Power Sources 134 (2004) 277–292.
[4] G.L. Plett, J. Power Sources 161 (2006) 1369–1384.
[5] R. Xiong, F. Sun, Z. Chen, H. He, Appl. Energy 113 (2014) 463–476.
[6] J. Kim, S. Lee, B.H. Cho, IEEE Trans. Power Electron. 27 (2012) 436–451.
[7] D. Andre, C. Appel, T.S. Guth, D.U. Sauer, J. Power Sources 224 (2013) 20–27.
[8] Z. Chen, C.C. Mi, Y. Fu, J. Xu, X. Gong, J. Power Sources 240 (2013) 184–192.
[9] W. He, N. Williard, M. Osterman, M. Pecht, J. Power Sources 196 (2011) 10314–10321.
[10] X. Hu, S.E. Li, Z. Jia, B. Egardt, Energy 64 (2014) 953–960.
[11] S.M. Rezvanizaniani, Z. Liu, Y. Chen, J. Lee, J. Power Sources 256 (2014) 110–124.
[12] M. Dubarry, C. Truchot, M. Cugnet, B.Y. Liaw, K. Gering, S. Sazhin, D. Jamison, C. Michelbacher, J. Power Sources 196 (2011) 10328–10335.
[13] M. Dubarry, C. Truchot, B.Y. Liaw, K. Gering, S. Sazhin, D. Jamison, C. Michelbacher, J. Power Sources 196 (2011) 10336–10343.
[14] M. Dubarry, C. Truchot, B.Y. Liaw, J. Power Sources 219 (2012) 204–216.
[15] M. Dubarry, B.Y. Liaw, J. Power Sources 194 (2009) 541–549.
[16] K. Honkura, K. Takahashi, T. Horiba, J. Power Sources 196 (2011) 10141–10147.
[17] I. Bloom, J. Christophersen, K. Gering, J. Power Sources 139 (2005) 304–313.
[18] I. Bloom, J.P. Christophersen, D.P. Abraham, K.L. Gering, J. Power Sources 157 (2006) 537–542.
[19] I. Bloom, L.K. Walker, J.K. Basco, D.P. Abraham, J.P. Christophersen, C.D. Ho, J. Power Sources 195 (2010) 877–882.
[20] D. Kim, S. Park, O.B. Chae, J.H. Ryu, Y.-U. Kim, R.-Z. Yin, S.M. Oh, J. Electrochem. Soc. 159 (2012) A193–A197.
[21] K.A. Walz, C.S. Johnson, J. Genthe, L.C. Stoiber, W.A. Zeltner, M.A. Anderson, M.M. Thackeray, J. Power Sources 195 (2010) 4943–4951.
[22] Y. Liu, X. Li, H. Guo, Z. Wang, Q. Hu, W. Peng, Y. Yang, J. Power Sources 189 (2009) 721–725.
[23] X. Li, Y. Xu, C. Wang, J. Alloys Compd. 479 (2009) 310–313.
[24] K.Y. Chung, K.B. Kim, Electrochim. Acta 49 (2004) 3327–3337.
[25] B. Deng, H. Nakamura, M. Yoshio, J. Power Sources 180 (2008) 864–868.
[26] J. Vetter, P. Novák, M.R. Wagner, C. Veit, K.C. Möller, J.O. Besenhard, M. Winter, M. Wohlfahrt-Mehrens, C. Vogler, A. Hammouche, J. Power Sources 147 (2005) 269–281.
[27] K. Amine, J. Liu, I. Belharouak, S.H. Kang, I. Bloom, D. Vissers, G. Henriksen, J. Power Sources 146 (2005) 111–115.
[28] K.L. Gering, S.V. Sazhin, D.K. Jamison, C.J. Michelbacher, B.Y. Liaw, M. Dubarry, M. Cugnet, J. Power Sources 196 (2011) 3395–3403.
[29] W. Shi, J. Jiang, W. Zhang, X. Li, J. Jiang, R. Jia, Automot. Eng. 35 (2013), 138–142, 151.
[30] M. Dubarry, C. Truchot, B.Y. Liaw, K. Gering, S. Sazhin, D. Jamison, C. Michelbacher, J. Electrochem. Soc. 160 (2013) A191–A199.
[31] X. Han, M. Ouyang, L. Lu, J. Li, Y. Zheng, Z. Li, J. Power Sources 251 (2014) 38–54.
[32] C.K. Huang, J.S. Sakamoto, J. Wolfenstine, S. Surampudi, J. Electrochem. Soc. 147 (2000) 2893–2896.